


# On the Use of CFRP Sheets for the Seismic Retrofitting of Masonry Walls and the Influence of Mechanical Anchorage

**Journal Article****Author(s):**

Bischof, Patrick; Suter, René; [Chatzi, Eleni](#) ; Lestuzzi, Pierino

**Publication date:**

2014-07-10

**Permanent link:**

<https://doi.org/10.3929/ethz-b-000164260>

**Rights / license:**

[Creative Commons Attribution 3.0 Unported](#)

**Originally published in:**

Polymers 6(7), <https://doi.org/10.3390/polym6071972>

Article

## On the Use of CFRP Sheets for the Seismic Retrofitting of Masonry Walls and the Influence of Mechanical Anchorage

Patrick Bischof <sup>1,\*</sup>, René Suter <sup>1</sup>, Eleni Chatzi <sup>2</sup> and Pierino Lestuzzi <sup>3</sup>

<sup>1</sup> Institute of Construction and Environment, University of Applied Sciences (UAS), Fribourg 1705, Switzerland; E-Mail: rene.suter@hefr.ch

<sup>2</sup> Institute of Structural Engineering, Swiss Federal Institute of Technology Zurich (ETHZ), Zurich 8093, Switzerland; E-Mail: chatzi@ibk.ethz.ch

<sup>3</sup> Applied Computing and Mechanics Laboratory IMAC, École Polytechnique Fédérale de Lausanne (EPFL), Lausanne 1015, Switzerland; E-Mail: pierino.lestuzzi@epfl.ch

\* Author to whom correspondence should be addressed; E-Mail: patrick.bischof@rothpletz.ch; Tel.: +41-31-330-84-65; Fax: +41-31-330-84-85.

Received: 9 April 2014; in revised form: 25 June 2014 / Accepted: 1 July 2014 /

Published: 10 July 2014

---

**Abstract:** This work reports the outcomes of an extensive experimental campaign on the retrofitting of masonry walls by means of carbon fiber reinforced polymer (CFRP) sheets, carried out at University of Applied Sciences (UAS) Fribourg. In the first stage, static-cyclic shear tests were conducted on the masonry walls, followed by a second stage of tensile tests on alternative configurations of mechanical anchorage so as to assess the effects on the structural response and to identify the associated limits. In the static-cyclic shear tests, it was found that the resistance of masonry walls retrofitted with CFRP sheets was improved by up to 70%, and the deformability was improved by up to 10% in comparison to the un-retrofitted specimens. The experimental tests conducted on alternate configurations of mechanical anchorages indicate that the tested materials and configurations rely heavily on details. The sensitivity of CFRP sheets to edges, non-uniformities on any adherend, and bonding defects can cause premature CFRP failure and, hence, pose problems for the efficient design of a retrofitting scheme. As indicated by the results of this investigation, effective anchorage can be achieved when eccentric loading of the mechanical anchorage is avoided and a smooth bonding surface is guaranteed.

**Keywords:** retrofitting; masonry; walls; carbon fiber reinforced polymer (CFRP) sheets; bonding; mechanical anchorage; composite materials

---

## 1. Introduction

In Europe, masonry buildings constitute a particularly large portion of existing building patrimony. Issues pertaining to the condition assessment of these structures are well documented in the literature. The structural walls of these buildings have been principally designed to resist gravity loads [1]. However, the horizontal loads induced by earthquake loading result in the development of in-plane and out-of-plane forces [2]. Recent work by Salamanpour *et al.* [3] indicates that performance of unreinforced masonry (URM) in structurally-designed low-rise URM buildings may be considered adequate for the category of ordinary buildings even in regions with appreciable seismic hazard. Nevertheless, the recent seismic events of Modena, 2012, Christchurch, 2011, and L'Aquila, 2009 [4–9], which not only caused extended material damage but also significant human toll, have critically pointed out the urgent need for appropriate strengthening of existing masonry structures. As before with the Loma Prieta and Northridge earthquakes, these losses resulting from such catastrophic events prompt the earthquake engineering community to embrace the concept of performance-based earthquake engineering [10,11] and investigations on the performance of masonry structures under earthquake loading [12].

In Switzerland, the need for updating the design standards came with the Swiss norm series of 2003 [13], where the required level of safety was adjusted to Eurocode 8 and the seismic risk zones were redefined relying on the most recent seismologic knowledge [14]. As a result, a large number of buildings in Switzerland constructed prior to 2003 are incapable of withstanding the updated design earthquake. Therefore, strengthening and retrofitting methodologies are deemed crucial. As masonry structures are difficult to model due to the multiple phases of the material and the numerous constituents involved [15,16], investigations inevitably have to initiate and rely on experimental tests. Lourenço *et al.* [17] presents a new construction system for masonry buildings using concrete block units and trussed reinforcement, validated through shaking table tests.

Retrofitting existing masonry buildings by means of fiber reinforced polymer (FRP) is at this point a frequently implemented strengthening solution. Schwegler [18] elaborates the idea of retrofitting masonry by means of pre-stressed FRP-laminates and conducted studies on the mechanical anchorage of these laminates. Triantafillou [19] presents a systematic analysis of the short-term strength of masonry walls, strengthened with externally bonded FRP laminates. ElGawady *et al.* [20,21] test different types of FRP laminates and sheets, including different materials, on their performance when retrofitting URM walls. Prota *et al.* [22] assess the available design formulas for in-plane shear behavior of retrofitted masonry walls and compare them with their experimental data. Kalali and Kabir [23] study the cyclic behavior of perforated masonry walls strengthened with glass fiber reinforced polymers. Fuggini *et al.* [24] numerically investigate the use of a quadri-axial polymeric textile for the strengthening of masonry walls. Mojsilovic *et al.* [25] discuss the strengthening of URM walls with prefabricated, pre-stressed elements for improving structural behavior and performance under cyclic

horizontal loading. A higher ductility and larger energy dissipation capacity of strengthened walls (compared to the URM walls) is demonstrated. A comprehensive review on the use of composites as strengthening materials can be found in the work of Triantafillou and Fardis [26] as well as Zhuge [27]. The FRP solution is attractive, since retrofitting can be performed quickly and without deep interventions in the load carrying structure of the building as would be necessary for example, when masonry walls are substituted by reinforced concrete (RC)-walls. Various types incorporating different materials, forms, orientations (uni- or bidirectional) of FRP are available (e.g., [28]).

At University of Applied Sciences (UAS) Fribourg, the retrofitting of masonry walls has developed into a major research focus since 2007. Theoretical studies and experimental campaigns at UAS Fribourg have mainly focused on the use of high performance fibers (carbon, glass and aramid) in different applications, including [29,30]. Within an extended research campaign labeled AGP 21159, “Seismic retrofitting of masonry walls”, retrofitted URM walls were subjected to a series of tests. In what follows, a systematic analysis is presented based on the outcomes of the extensive experimental campaign and guidelines are provided on the practical implementation of such retrofitting solutions.

## 2. The Research Project

### 2.1. Experimental Series

This paper reports the outcomes of an experimental campaign aiming to quantify the seismic capacity of URM walls, the benefit of CFRP retrofitting and the influence that anchorage holds in the performance of the retrofitting solution. The results of these tests are valuable in engineering practice as they discuss in detail the effectiveness of a frequently used solution, which nonetheless is very infrequently tested. Series MR-B reports the outcomes of experimental tests on URM walls retrofitted by means of CFRP sheets under static-cyclic loading. In Series AT-H, AT-F and AT-C, the mechanical anchorage of CFRP sheets by means of aluminum or steel profiles was studied under monotonic tensile loading. Kalfat *et al.* [31] and Grelle and Sneed [32] point out that metallic anchorages proved to be an effective anchorage device. Initial investigations and studies of ElGawady *et al.* [20] demonstrate the significant influence of the anchorage configuration on the overall system response. Massive metallic profiles are often used in practice for anchoring the CFRP sheets although they are not needed. Ceroni *et al.* [33] provide some insights in the mechanical anchorage of CFRP sheets. This article aims to study the mechanical anchorage system by metallic profiles as well as re-dimension and optimize the metallic profiles. Nigro *et al.* [34] show that that the cyclic loading of CFRP sheets-to-concrete-joints does not substantially affect debonding loads in the case of bond lengths exceeding the effective bond length. Additionally to the experimental series, approximate numerical analyses on the anchorage of CFRP sheets on metal were performed in order to gain a better insight on the workings of the bonding mechanism.

### 2.2. Material Properties

In all of the experimental series, standard Swiss clay brick masonry as defined in the Swiss code SIA 266 [12] was used with bricks with the following dimensions: length: 300 mm, height: 190 mm, width: 150 mm. Compression tests on single clay bricks and compression and bending tests on the

mortar have been performed. The tested mean values of the material properties are given in Table 1. Two different CFRP sheets were used for the retrofits throughout the four experimental series: S&P C-Sheet 240-200 g/m<sup>2</sup> and S&P C-Sheet 240-400 g/m<sup>2</sup>. For the mechanical anchorage, either steel or aluminum profiles were applied. To assure intimate contact between adherend (mechanical anchorage) and adhesive, the adherend was grit-blasted and cleaned before bonding (Fernando *et al.* [35] give recommendations on the surface preparation of steel adherends). The material properties of the CFRP sheets and the adhesive used in the experiments are given in Table 2.

**Table 1.** Properties for masonry walls.

Material	Material Properties	
Clay brick	Compression strength $f_{bk}$ (N/mm <sup>2</sup> )	41.0
Mortar for clay brick	Flexural tension strength $f_{tk}$ after 28 days (N/mm <sup>2</sup> )	3.1
	Compression strength $f_{mk}$ after 28 days (N/mm <sup>2</sup> )	10.2

**Table 2.** Properties of carbon fiber reinforced polymer (CFRP) sheets (linear-elastic range) and adhesive given by manufacturer [36] based on the experiment report of [37].

CFRP Sheets	S&P C-Sheet 240-200 g/m <sup>2</sup>	S&P C-Sheet 240-400 g/m <sup>2</sup>
Elastic modulus E (N/mm <sup>2</sup> )	240,000	240,000
Elongation at rupture (theoretical) (%)	1.55	1.55
Theoretical ultimate tensile strength $f_u$ (N/mm <sup>2</sup> )	3,800 <sup>1</sup>	3,800 <sup>1</sup>
Theoretical design cross section 1 m width (mm/m)	117	234
Adhesive	S&P Resicem	
Elastic modulus E at +20°C. (N/mm <sup>2</sup> )	4,820	
Tensile strength after 14 days $f_u$ (N/mm <sup>2</sup> )	22	
Pull off strength on concrete (N/mm <sup>2</sup> )	>4 (failure in concrete)	
Pull off strength on steel (N/mm <sup>2</sup> )	>10.6	

Note: <sup>1</sup> The manufacturer recommends limiting the design tensile stress for axial loading to ~1200 N/mm<sup>2</sup> (limit strain at ultimate state  $\epsilon_u$  0.6%).

### 3. Static–Cyclic Shear Tests on Retrofitted Masonry Walls

#### 3.1. Test Set-Up

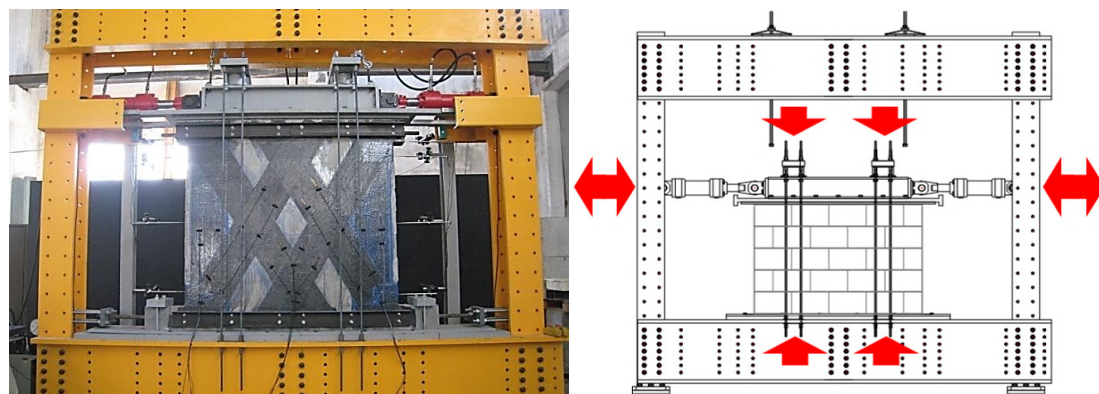
The static-cyclic shear load tests in Series MR-B were carried out on a set-up specifically designed for this research project (Figure 1). This test set-up allowed for the application of vertical and horizontal forces simultaneously with fixed-fixed boundary conditions. The static-cyclic test was performed as follows:

- Firstly, a vertical load of 135 kN, corresponding to a distributed load of 0.5 N/mm<sup>2</sup>, was applied by two hydraulic actuators with a capacity of 1000 kN each. This vertical load was kept approximately constant during the entire test. The difference of the medium vertical load caused by cyclic horizontal loading was 0.1 N/mm<sup>2</sup> maximum.
- Secondly, a horizontal load was applied by two actuators with a capacity of +200/–300 kN each. Both were independently connected to an individual hydraulic system. The horizontal force was progressively and alternatively increased on each side, until the first crack occurred.

The test was then driven by deformation until the ultimate limit state was reached and complete failure occurred.

The masonry walls (height: 1400 mm, length: 1800 mm, thickness: 150 mm) were built between two RC-beams (length: 2000 mm, height: 200 mm, width: 150 mm), which represented RC-slabs below and above the masonry wall. The carbon mesh was mechanically anchored with standardized U-formed steel profiles (UPN 120, height: 120 mm), which were themselves mechanically fastened in the RC-beams. The vertical and the horizontal load were applied through the upper RC-beam.

**Figure 1.** Set-up for static-cyclic shear load tests.



An extensive instrumentation was utilized:

- Two pressure sensors on both hydraulic systems
- Two load cells on the horizontal cylinders
- Several displacement measurements by linear variable differential transformers (LVDT)
- Several strain measurements by means of strain gauges (SG)

The number and placement of SG varied as a function of the tested retrofitting configuration.

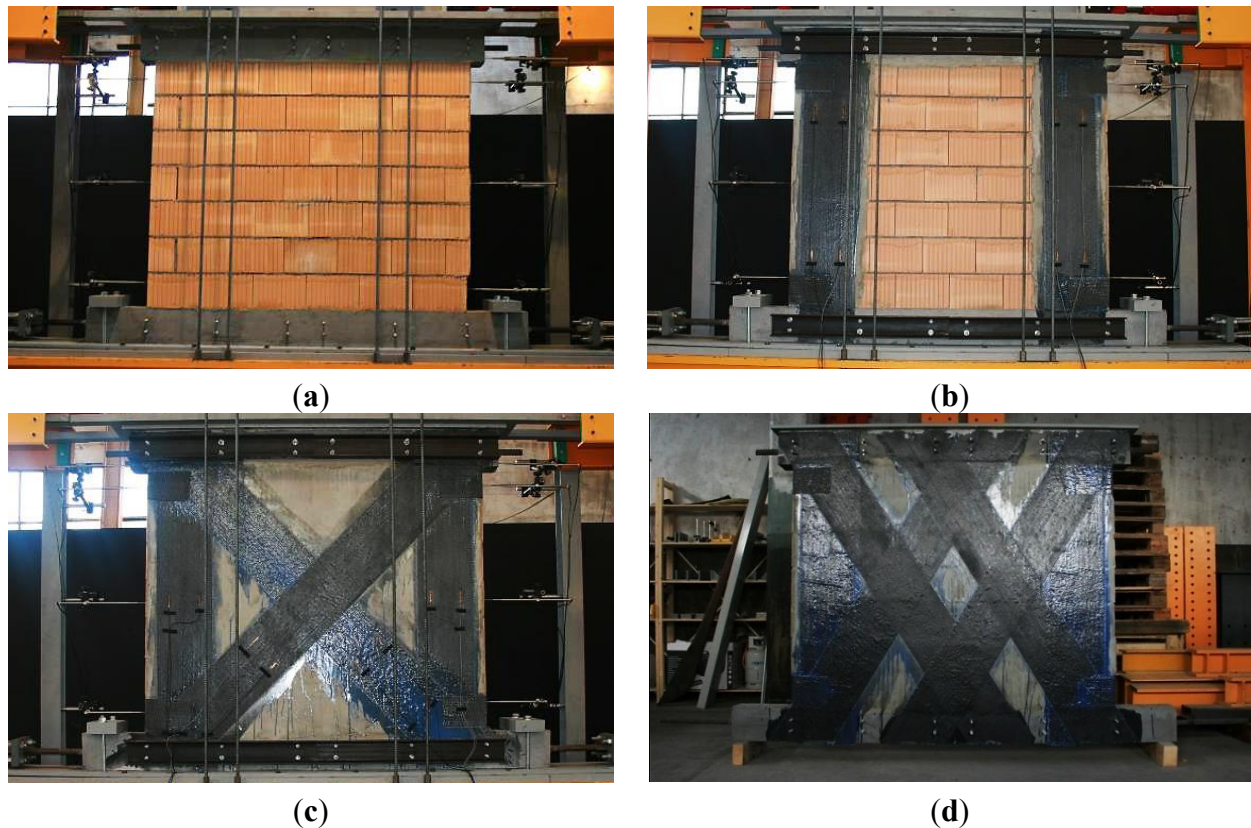
### 3.2. Experimental Program

In Series MR-B, static-cyclic tests on five masonry walls were conducted. Four walls were retrofitted by bonded CFRP sheets (C-sheets 200 g/m<sup>2</sup> and C-sheets 400 g/m<sup>2</sup>, both with width: 300 mm), whereas one served as a reference wall without retrofit. The reinforcement was only applied on one face of each wall. Even though this creates a small eccentricity, the influence on the shear capacity and the deformability is negligible [38]. The tested configurations are summarized in Table 3 and Figure 2.

**Table 3.** Tested configurations of retrofitted masonry walls in Series MR-B.

Specimen	Type of CFRP Sheet	Retrofit Configuration
MR-B1	-	Reference wall, no retrofit
MR-B2	C-sheets 200 g/m <sup>2</sup>	Two vertically bonded CFRP sheets
MR-B3	C-sheets 200 g/m <sup>2</sup>	Two vertically and two diagonally (45°) bonded CFRP sheets
MR-B4	C-sheets 400 g/m <sup>2</sup>	Two vertically and two diagonally (45°) bonded CFRP sheets
MR-B5	C-sheets 200 g/m <sup>2</sup>	Two vertically and four diagonally (60°) bonded CFRP sheets

**Figure 2.** Different configurations of carbon mesh for retrofitting masonry walls in Series MR-B. (a) MR-B1; (b) MR-B2; (c) MR-B3 (200 g/m<sup>2</sup>)/MR-B4 (400 g/m<sup>2</sup>); (d) MR-B5.



### 3.3. Test Results

A summary of the maximum applied load and the maximum reached deformation at the top of the wall is given in Table 4. The load-displacement curves of the retrofitted masonry walls in Series MR-B are shown in Figure 3.

**Table 4.** Horizontal force and maximum displacement at the top of the wall in Series MR-B.

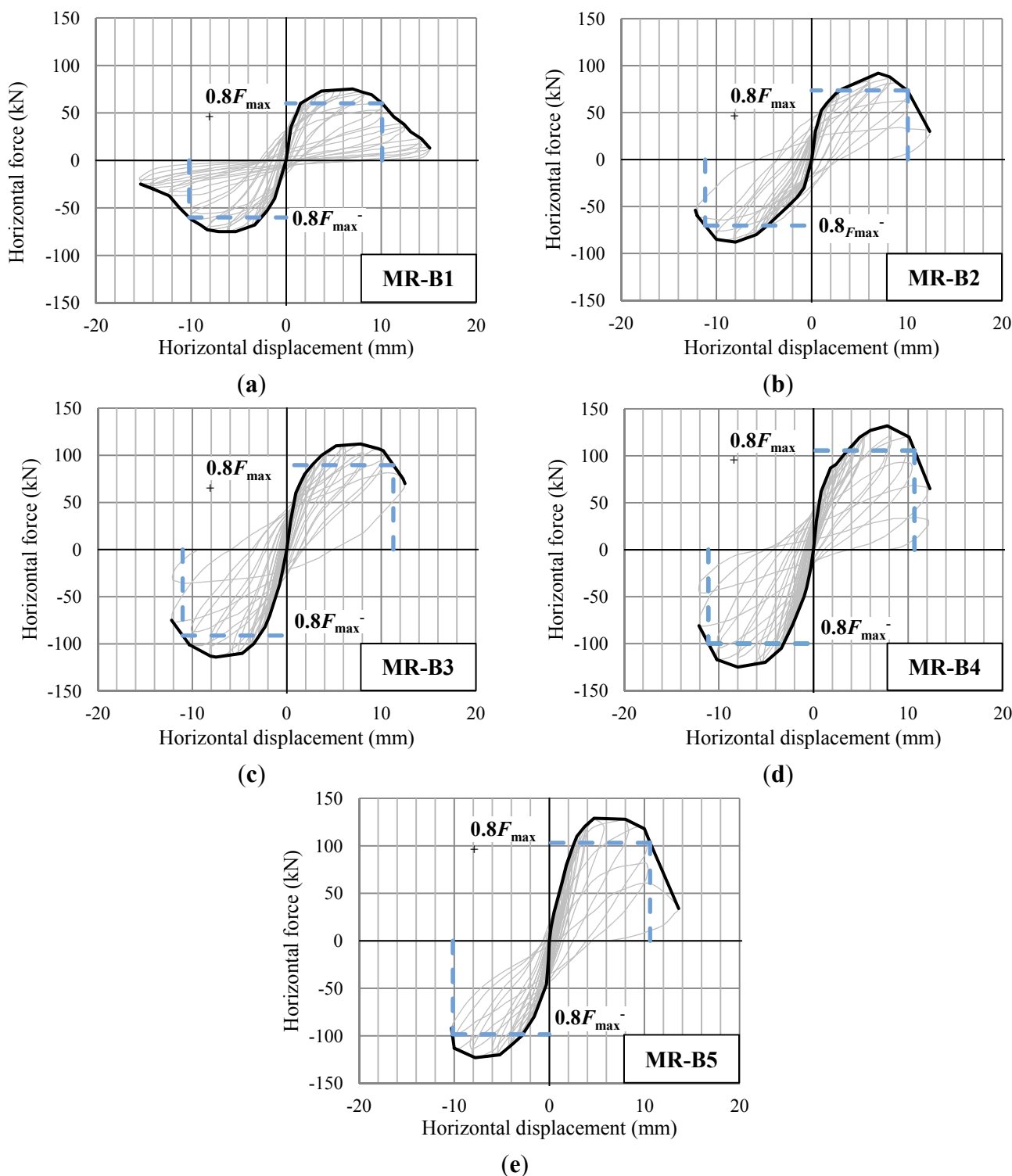
Specimen	$F_{\max}^+$ (kN)	$F_{\max}^-$ (kN)	Comparison to Reference Wall	$0.8F_{\max}^+$ (kN)	$0.8F_{\max}^-$ (kN)	$\delta_u^+$ (mm)	$\delta_u^-$ (mm)	Comparison to Reference Wall
MR-B1	75.2	76.8	100%	60.2	61.4	10.1	10.2	100%
MR-B2	91.7	89.0	119%	73.4	71.2	10.1	11.2	105%
MR-B3	111.9	113.7	148%	89.5	91.0	11.3	11.0	110%
MR-B4	131.8	125.3	169%	105.4	100.2	10.7	11.1	107%
MR-B5	129.9	125.0	168%	103.9	100.0	10.6	10.1	102%

The behavior documented in the experimental Series MR-B demonstrates an improvement of the performance of retrofitted masonry walls through the increase of the horizontal load capacity by almost up to 70% and of the deformation capacity by up to 10% in comparison to the reference wall. The increase of deformation capacity might appear as rather small. However, in Switzerland, buildings normally are rather stiff. Hence, the seismic response of a typical Swiss building is often represented by the maximum amplification. As the design ground acceleration is moderate (0.6–1.6 m/s<sup>2</sup>), an



increase of the load capacity might be a good solution for retrofitting a building. Nevertheless, various studies exist on retrofitting masonry walls by means of CFRP sheets, also elaborating on the deformation capacity obtained through different retrofit configurations employing various materials (e.g., in [20,21]).

**Figure 3.** Load-displacement curves in Series MR-B. (a) MR-B1; (b) MR-B2; (c) MR-B3; (d) MR-B4 and (e) MR-B5.

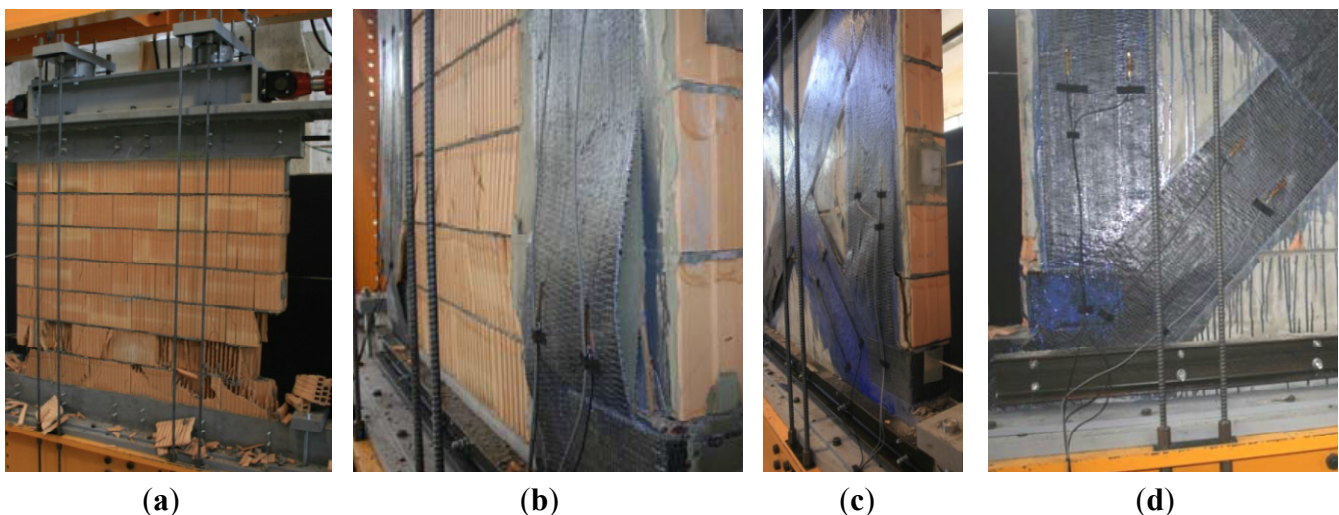




All five walls behaved very stiffly in the beginning. At a horizontal load of 60 kN and a horizontal deformation of 1 mm, cracking initiated in specimens MR-B1 and MR-B2 with an angle of approximately  $60^\circ$  with respect to the horizontal, which corresponds to the inclination of the diagonal compression strut. In specimens MR-B3 to MR-B5 with diagonal shear reinforcement, the masonry remained without cracks up to a horizontal force of approximately 80 kN. In specimen MR-B3, the angle of the cracks shifted from  $60^\circ$  to  $45^\circ$  according to the diagonally applied CFRP sheets.

In all cases, cracking initiated at the lower angles of the masonry wall. In specimens MR-B4 and MR-B5, the wall slid in the horizontal joint above the lowest brick layer (see Figure 4d). Failure always occurred when the masonry wall reached its compression capacity due to the superposition of the diagonal compression strut and the vertical force (Figure 4 for specimens MR-B1, MR-B2, MR-B3, and MR-B4). Compression failure of masonry happened at the lower angles where the vertical load acting on the wall without seismic loading and the vertical component induced by the horizontal force from seismic loading superpose. In the case of specimen MR-B2 as well as of specimen MR-B3, the CFRP sheet debonded from the masonry surface (Figure 4b) and, hence, acted as an external tension strut anchored by steel profiles in the following load circles. The stress determined from the maximum measured strain in specimen MR-B2 reached almost  $1000 \text{ N/mm}^2$  and was not uniformly distributed over the whole sheet length. With the retrofit in specimen MR-B3, the fiber stresses are more uniformly distributed than in wall MR-B2. It was observed that the tensile stresses were higher in the diagonally applied sheets than in the vertically applied sheets. Stronger retrofits, as executed in specimens MR-B4 and MR-B5, caused reduced cracking because the CFRP sheets spread the tensile forces over a larger surface. Furthermore, the CFRP sheets remained almost perfectly bonded over the whole loading process due to reduced fiber stresses.

**Figure 4.** Failed specimens in Series MR-B. (a) MR-B1; (b) MR-B2; (c) MR-B3; and (d) MR-B4.

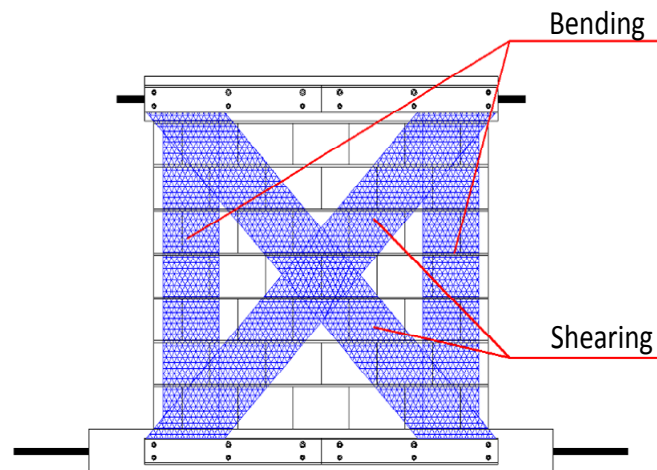


The vertical reinforcement increases the bending strength and assists in resisting rocking effects whereas the diagonally applied reinforcement strongly enhances the shear capacity. The closer the inclination angle of the diagonal carbon strips moves from  $45^\circ$  to  $90^\circ$  with respect to the horizontal, the less the shear capacity is enhanced. By doubling the fiber cross section, the shear resistance was only

increased by about 13% until failure occurred in the lower angles of the masonry walls due to compression failure of the masonry.

The analysis of this tension and compression strut creates the possibility to design according to the truss analogy or according to stress fields (Figure 5).

**Figure 5.** State of stress in retrofitted masonry wall.



The ACI (American Concrete Institute) has published recommendations to calculate the contribution of diagonal FRP sheets on masonry walls [39]. Furthermore, the Italian CNR (National Research Committee) has established a guidance to evaluate the mean debonding fiber stresses of vertical and horizontal FRP sheets [40].

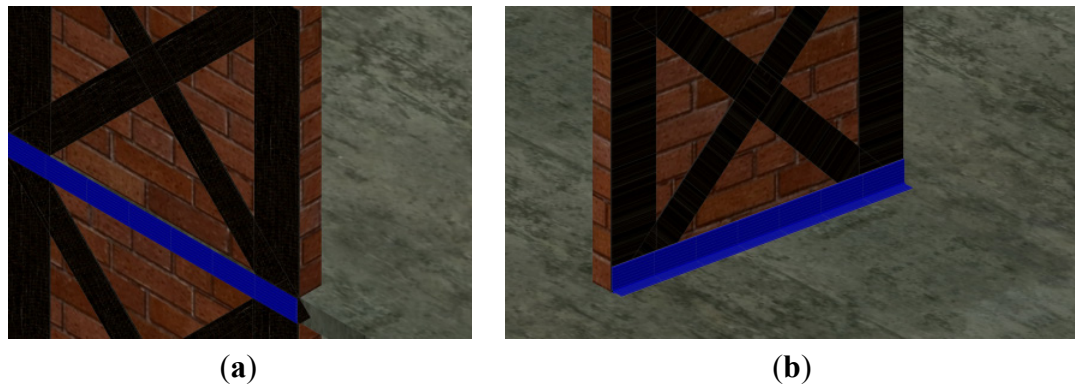
The mechanical anchorage of the CFRP sheets is of high importance. The high tensile capacity of carbon fibers can only be exploited when the fibers are well anchored. In Series MR-B, the mechanical anchorage was imposed by heavy U-formed steel profiles, which were fixed in the concrete beams. Even though this kind of mechanical anchorage was not the critical element due to over-dimensioning, very little is known about its behavior and the potential for optimization was not elaborated. Therefore, an experimental campaign on mechanical anchorage was initiated in order to better understand the extent of its influence on overall structural behavior.

#### 4. Influence of Mechanical Anchorage

##### 4.1. Implementation

Depending on the location of URM walls in buildings that ought to be retrofitted, two different implementations of mechanical anchorages are possible. For exterior walls, the carbon mesh is anchored in the slab edge (Figure 6a) whereas for interior walls, the carbon mesh is anchored in the slab perpendicular to the wall (Figure 6b). Series AT-F was conducted to study the former problem whereas Series AT-C was conducted to study the latter.

**Figure 6.** Implementation of mechanical anchorage (a) for exterior walls and (b) for interior walls.

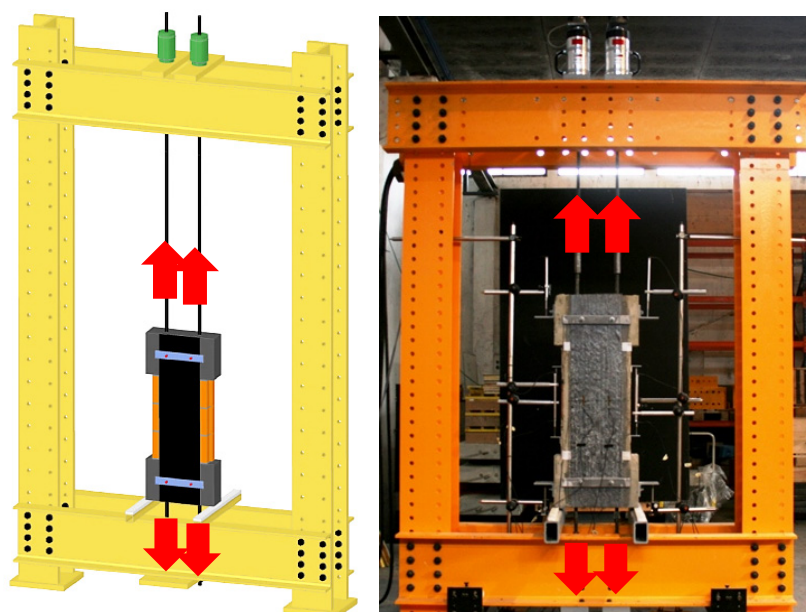


## 4.2. Experimental Studies

### 4.2.1. Test Set-Up

The test set-up for the static tensile tests on the mechanical anchorage of CFRP sheets consists of a heavy steel frame. A hydraulic system incorporating one manually controlled pressure pump and two hydraulic cylinders was used to apply tension to the CFRP sheet. The two hydraulic cylinders make it possible to load two strong threaded steel rods. These two steel rods were connected to an upper rectangular hollow section (RHS) profile in Series AT-H, to a 150 mm diameter aluminum cylinder in Series AT-C (apart from specimen AT-C9), and to a concrete block in Series AT-F and specimen AT-C9 of Series AT-C (Figure 7). In every experiment, two identical mechanical anchorages were applied on both sides of the test specimen for equilibrium reasons. The instrumentation included several displacement measurements by means of linear variable differential transformers (LVDT) and strain measurements by means of strain gauges (SG). The instrumentation is shown in the following subsections for each experimental series separately.

**Figure 7.** Set-up for static tensile load tests on mechanical anchorage (here: Series AT-F)



4.2.2. Series AT-H

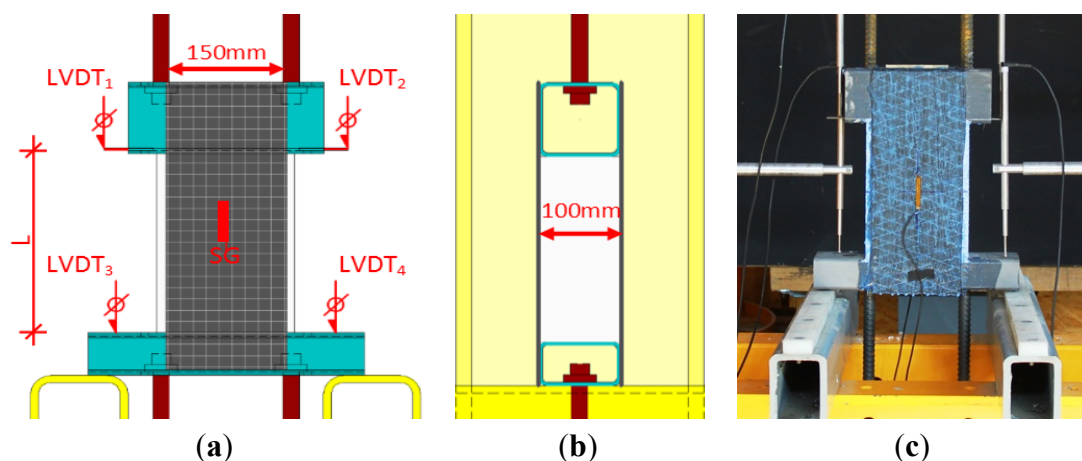
Experimental Program

For Series AT-H, double shear tests were conducted. The characteristics of Series AT-H are given in Table 5. The test specimens were made of two steel rectangular hollow section (RHS) profiles with a 250 mm long and 100 mm wide polystyrene cuboid in between, bonded with 150 mm wide CFRP sheets at the front and back side (Figure 8). The lower RHS profile was anchored with steel rods in the heavy steel frame while the upper RHS profile was pulled (principle of loading and anchoring as shown for Series AT-F in Figure 7). The CFRP sheets, thus, transferred the pulling force from one RHS profile to the other. The upper RHS profile was larger than the lower one so as to assure a longer bond length at the upper profile (lower anchorage profile is given in Table 5). Therefore, failure would occur at the lower RHS profile if the bonded length was smaller than the effective bond length, beyond which the adhesive joint load capacity does not increase. The bonded length varied between 41.1 and 85 mm, depending on the anchorage profile. A shorter bonded length than 41.1 mm was not tested due to structural reasons (anchorage of lower RHS profile). The curvature of the RHS profiles was filled with Silicone in specimens AT-H1 to AT-H4 and with Sikaflex<sup>®</sup>-11 FC in specimens AT-H9 to AT-H12 in order to guarantee a smooth bonding surface, which is an important criterion to prevent local stress concentrations and, hence, premature failure.

Table 5. Characteristics of Series AT-H.

Specimen	Type of C-Sheet	Anchorage Profile (Lower RHS Profile)	Bonded Length (mm)
AT-H1	240-200 g/m <sup>2</sup>	RHS 100/60/5 (width/height/thickness)	45.0
AT-H2	240-200 g/m <sup>2</sup>	RHS 100/60/5	45.0
AT-H3	240-200 g/m <sup>2</sup>	RHS 100/100/5	85.0
AT-H4	240-200 g/m <sup>2</sup>	RHS 100/100/5	85.0
AT-H9	240-400 g/m <sup>2</sup>	RHS 100/60/6.3	41.1
AT-H10	240-400 g/m <sup>2</sup>	RHS 100/60/6.3	41.1
AT-H11	240-400 g/m <sup>2</sup>	RHS 100/100/6.3	81.1
AT-H12	240-400 g/m <sup>2</sup>	RHS 100/100/6.3	81.1

Figure 8. (a,b) Model with instrumentation of specimen in Series AT-H in view and sectional drawing; and (c) specimen of Series AT-H.



The instrumentation is given in Figure 8a. The double shear tests basically aimed to give an idea of the applicable load on CFRP sheet-steel-joints. As double shear tests rely on symmetry and become unstable after one side fails, basically two bonded surfaces were tested on ultimate load capacity with one specimen resulting in the failure of the weaker one. However, an exact study of the bonding behavior would require a more intensive instrumentation with SG on the bonded surface.

### Test Results

In Table 6, the test results of Series AT-H are given. If bond shear stress is assumed to be uniformly distributed over the whole bonded surface, the maximum load of 138 kN in test AT-H10 corresponds to a bond shear stress of 11.2 N/mm<sup>2</sup>. Considering the actual shear bond transfer over the effective bond length described by a hyperbolic behavior up to the maximum bond shear stress and a subsequent harmonic behavior, when assuming a bilinear bond-slip-model (which holds for linear adhesives, according to [41]), the maximum bond shear stress has to be significantly higher than the minimum value (10.6 N/mm<sup>2</sup>, see Table 2) given by the manufacturer for the adhesive S&P Resicem. The strains given in Table 6 represent  $\delta(F_{\max})/L$  and approximately correspond to the measured strains by SG. The strains slightly exceed the recommendations of the manufacturer at ultimate state (see Table 2).

Given the rather high maximum applied fiber tensile stresses reached in Series AT-H, the bonded length of 40 mm for the aluminum profiles, used as mechanical anchorage in Series AT-C and AT-F, can be considered as sufficiently long for both CFRP sheet 240-200 g/m<sup>2</sup> and CFRP sheet 240-400 g/m<sup>2</sup>.

**Table 6.** Test results of Series AT-H.

Specimen	$F_{\max}$ (kN)	$F_{\max}/R_u$ <sup>1</sup> (-)	$\sigma_{\max}$ (N/mm <sup>2</sup> )	$\delta(F_{\max})$ <sup>2</sup> (mm)	$\varepsilon(F_{\max})$ <sup>3</sup> (%)
AT-H1	51	0.38	1442	1.3	0.49%
AT-H2	71	0.53	2022	2.0	0.75%
AT-H3	62	0.47	1772	1.6	0.60%
AT-H4	70	0.53	2002	1.3	0.49%
AT-H9	120	0.45	1715	1.8	0.68%
AT-H10	138	0.52	1972	2.0	0.75%
AT-H11	137	0.51	1956	1.6	0.60%
AT-H12	110	0.41	1572	1.6	0.60%

Note: <sup>1</sup>  $R_u$  represents the theoretical ultimate tensile strength of the carbon fibers (fiber rupture).

<sup>2</sup> Displacement measurement between top LVDT (1, 2) and bottom LVDT (3, 4) (see Figure 8a); <sup>3</sup>  $\varepsilon(F_{\max})$  represents  $\delta(F_{\max})/L$ .

#### 4.2.3. Series AT-F

#### Experimental Program

For the specimens of Series AT-F, three masonry bricks were placed between two concrete blocks with encased threaded steel rods: two vertical rods for applying the test load and two horizontal rods for fastening the mechanical anchorage (aluminum profiles: thickness 15 mm, curvature 15 mm). The masonry and concrete surface was leveled and uniformed by applying a leveling compound. After



adding adhesive to the surface, 300 mm wide carbon fiber sheets were applied on the front and back side and the aluminum profiles were fastened (Figure 9). Table 7 summarizes the characteristics of Series AT-F.

**Figure 9.** (a,b) Model with instrumentation of specimen in Series AT-F in view and sectional drawing; and (c) CFRP sheet mechanically fixed by aluminum profile.

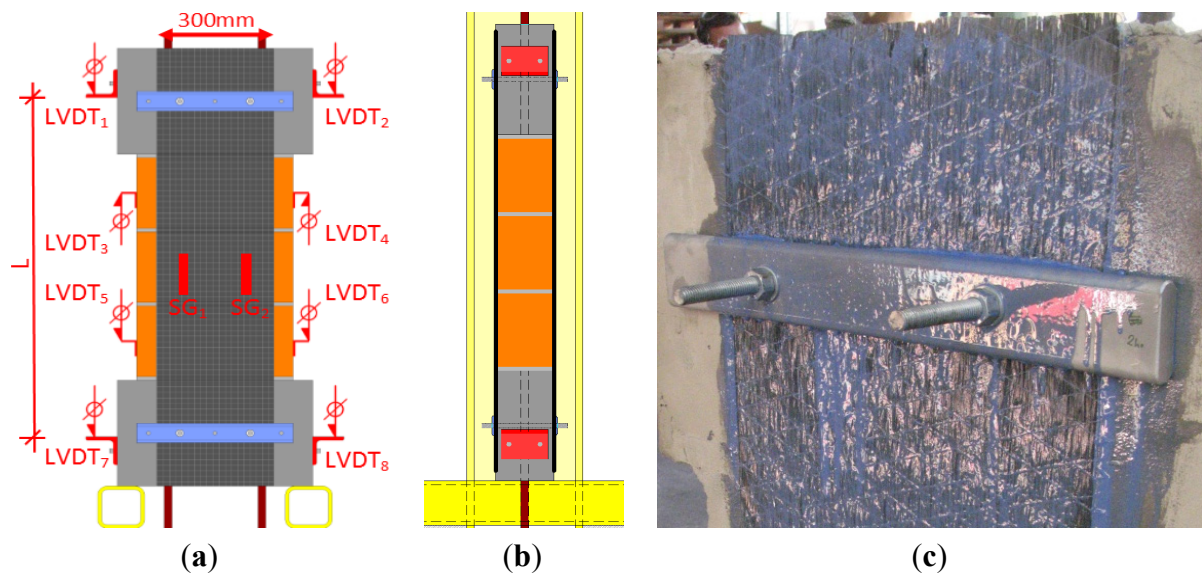


**Table 7.** Characteristics of Series AT-F.

Specimen	Type of C-Sheet	Anchorage Profile	Bonded Length (mm)
AT-F6	240-200 g/m <sup>2</sup>	S&P Aluminum profile	40.0
AT-F9	240-200 g/m <sup>2</sup>	S&P Aluminum profile	40.0
AT-F11	240-400 g/m <sup>2</sup>	S&P Aluminum profile	40.0
AT-F12	240-400 g/m <sup>2</sup>	S&P Aluminum profile	40.0

### Test Results

Table 8 shows test results of Series AT-F and Figure 10 shows the associated load-displacement curves (displacement between upper concrete block—LVDT 1 and 2—and lower concrete block—LVDT 7 and 8). In Figure 11, the stress determined from the maximum measured strain and the total stress ( $F/A_{\text{Fiber}}$ ) are compared. In Figure 12, specimens AT-F6, AT-F11, and AT-F12 are shown after complete failure and specimen AT-F9 is shown after bonding failure of the interface concrete-CFRP.

**Table 8.** Test results of Series AT-F.

Specimen	$F_{\text{max}}$ (kN)	$F_{\text{max}}/R_u^1$ (-)	$\sigma_{\text{max}}$ (N/mm <sup>2</sup> )	$\delta(F_{\text{max}})^2$ (mm)	$\epsilon(F_{\text{max}})^3$ (%)
AT-F6	123	0.46	1757	8.0	0.85%
AT-F9	145	0.54	2059	13.4	1.43%
AT-F11	150	0.28	1066	6.5	0.69%
AT-F12	165	0.31	1174	6.8	0.72%

Note: <sup>1</sup>  $R_u$  represents the theoretical ultimate tensile strength of the carbon fibers (fiber rupture).  
<sup>2</sup> Displacement measurement between top LVDT (1, 2) and bottom LVDT (7, 8) (see Figure 9a); <sup>3</sup>  $\epsilon(F_{\text{max}})$  represents  $\delta(F_{\text{max}})/L$ .

**Figure 10.** Load-displacement curves of Series AT-F. (a) C-Sheet 200 g/m<sup>2</sup>; (b) C-Sheet 400 g/m<sup>2</sup>.

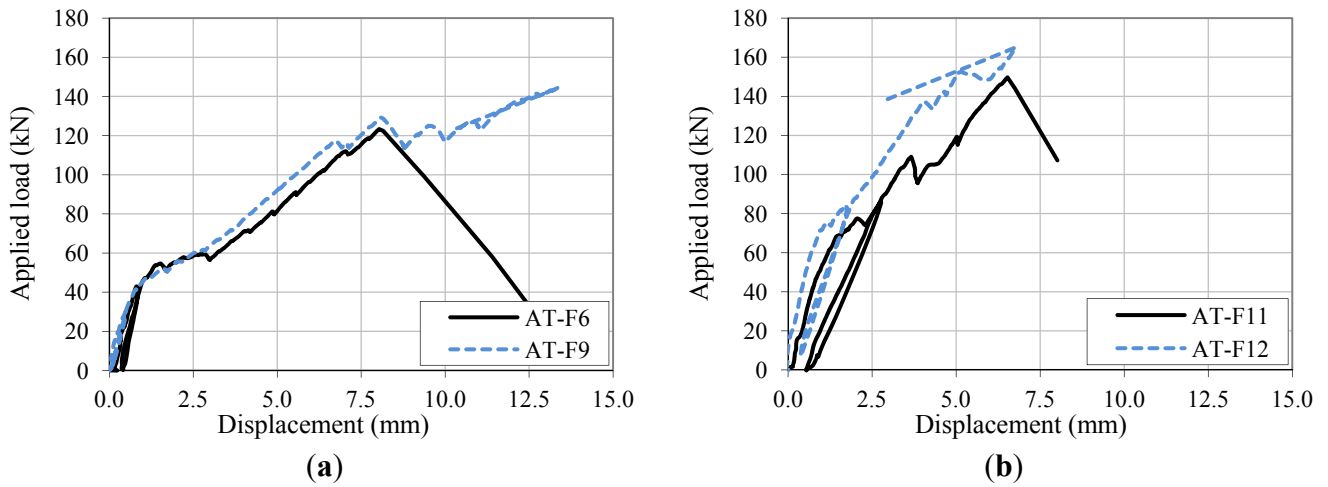


**Figure 11.** Comparison of measured fiber stress (strain gauges) and total stress ( $F/A_{Fiber}$ ) in Series AT-F.

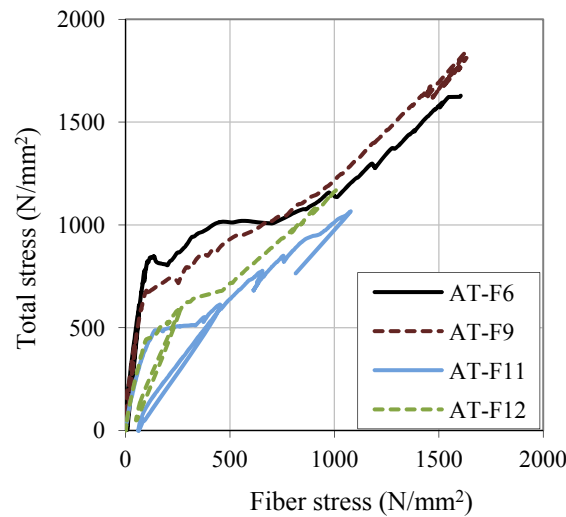
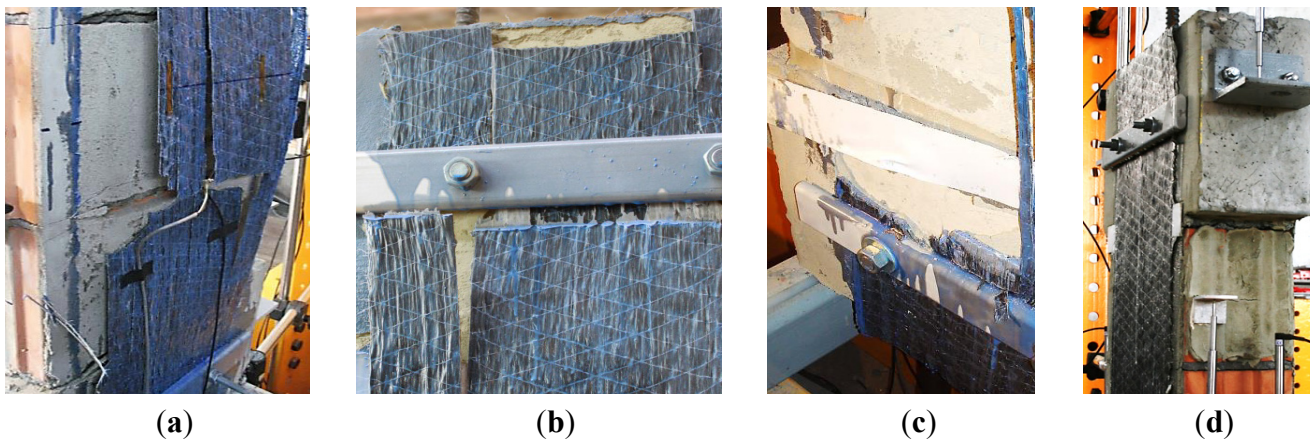


**Figure 12.** (a) Failed specimen AT-F6; (b) Failed specimen AT-F11; (c) Failed specimen AT-F12; and (d) Specimen AT-F9 before failure.



The test specimen is initially very stiff due to the tensile strength of the mortar that connects the concrete blocks and the masonry bricks (Figures 10 and 11), For the C-Sheet 200 g/m<sup>2</sup>, the mortar's



tensile failure obviously occurs at approximately the double fiber stress with respect to the C-Sheet 400 g/m<sup>2</sup>. After the mortar's failure, the load is completely transferred to the CFRP sheet. Fibers which are not perfectly arranged in the load direction either fail or orientate towards the load direction in a "transition phase" before all fibers are fully loaded (the curve in Figure 11 approaches a 45°-angle). The strains given in Table 8 represent  $\delta(F_{\max})/L$  and, apart from specimen AT-F9, approximately correspond to the measured strains by SG. In specimens AT-F9, AT-F11, and AT-F12, the CFRP sheet peeled from the concrete block. Both the joint between CFRP sheets and metallic mechanical anchorage, as well as between CFRP sheets and concrete, interact until the abrupt failure of the latter (Figure 12d). Afterwards, further load increase was possible. Consequently, the tensile strength of CFRP sheets can better be exploited by metallic mechanical anchorages than by bonding to concrete or masonry only. Debonding only occurred in specimen AT-F11, most probably because adhesive leaked from under the S&P aluminum profile before curing and left about a third of the contact surface between CFRP sheet and mechanical anchorage unbonded on both the front and the back side. Interestingly, experiment specimen AT-F9 showed a "quasi-ductile" behavior by repeated failure of fibers at an applied load around 120 kN (see Figure 10a).

In Series AT-H, the magnitude of applied fiber stresses, which could be mechanically anchored on steel profiles, was similar for both S&P C-Sheets 240-200 g/m<sup>2</sup> and S&P C-Sheets 240-400 g/m<sup>2</sup>. In Series AT-F, however, the specimens retrofitted with S&P C-Sheets 240-400 g/m<sup>2</sup> did not reach the expected level of load application, most probably due to stress concentrations as it seems from examining the failed test specimens (see Figure 12b,c). Small irregularities, e.g., adhesive bonding problems in specimen AT-F11, weaken the anchorage system and cause premature failure.

#### 4.2.4. Series AT-C

##### Experimental Program

For test specimens AT-C1 to AT-C8, a masonry brick was placed on an anchored reinforced concrete block. The CFRP sheets were pulled by an aluminum cylinder with 150 mm diameter (Figure 13). For test specimen AT-C9, two masonry bricks were placed between an upper, vertical concrete block and an anchored lower, horizontal concrete block (Figure 14). Aluminum profiles (thickness 15 mm, curvature 15 mm) bonded to the CFRP sheets and anchored in the upper, vertical concrete block were used for pulling the CFRP sheets. The configuration in specimen AT-C9 allowed for a uniformly bonded surface between the CFRP sheet and the concrete blocks as well as between the CFRP sheet and the masonry bricks. The masonry and concrete surfaces were leveled and uniformed by applying a leveling compound. For specimens AT-C1 to C8, a 300 mm wide carbon fiber sheet was applied, whereas for specimen AT-C9, a 200 mm wide carbon fiber sheet was applied.

The characteristics of Series AT-C are summarized in Table 9. In specimens AT-C1 to AT-C4 and AT-C9, steel rectangular hollow section (RHS) steel profiles were used for the mechanical anchorage of the CFRP sheet in the lower concrete block whereas in specimens AT-C5 to AT-C8, L-formed steel profiles (LNP) were used. The values after RHS indicate the width, the height, and the thickness of the profile and the values after LNP describe the length of the vertical arm, the length of the horizontal arm, and the thickness of the L-formed profile. Apart from specimens AT-C1 and AT-C9, the used

RHS profiles were cut in half resulting in L-shaped profiles with round edges (LNP profiles have sharp edges at the outer face). These round edges allow for the CFRP sheet to be bonded to both sides of these cut RHS profiles. Hence, the CFRP sheet undergoes a change of direction. In order to study the consequences caused by different magnitudes of diverting stresses in the curvature of the mechanical anchorage, the curvature radius was varied between set-ups (see Table 9).

The steel profile was vertically anchored in the concrete block with mechanical fasteners (dimensions given in Table 9) for specimens AT-C1 to AT-C8 and with steel rods encased in the concrete block for specimen AT-C9. For specimens AT-C2 to AT-C8, horizontal anchors (dimensions given in Table 9) were applied to avoid the turning effect brought about by the eccentricity of the loaded carbon fibers with respect to the vertical fasteners.

**Figure 13.** (a,b) Model with instrumentation of specimen in Series AT-C in view and sectional drawing; (c) Specimen of Series AT-C.

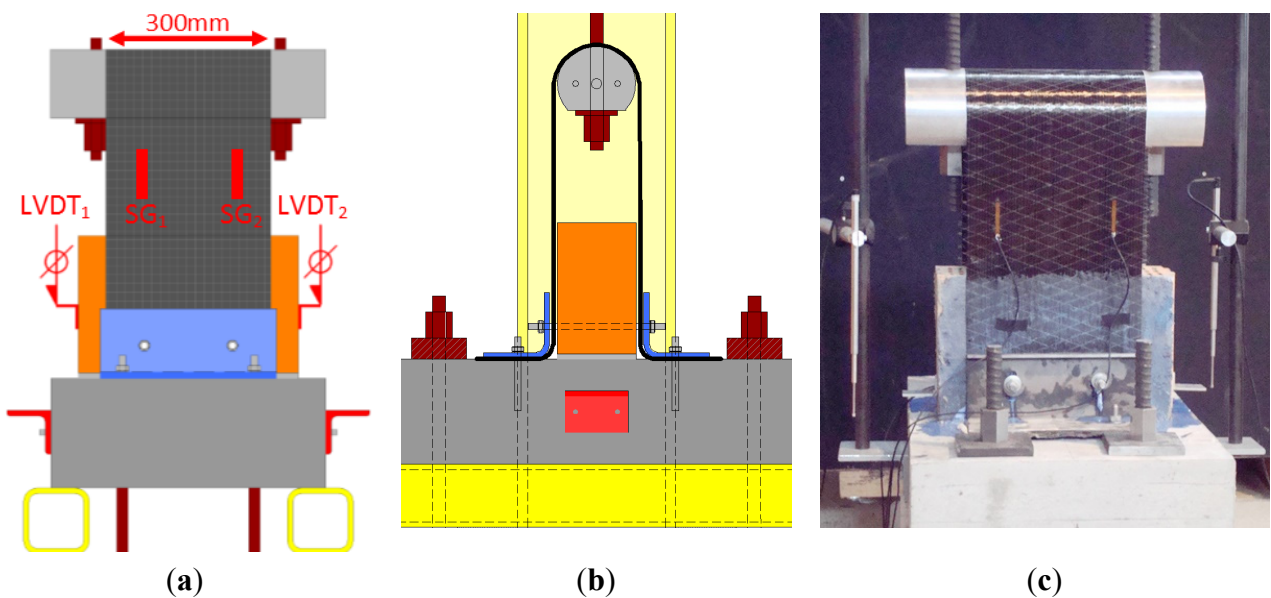


**Figure 14.** (a,b) Model with instrumentation of specimen AT-C9 in view and sectional drawing. (c) Specimen AT-C9.

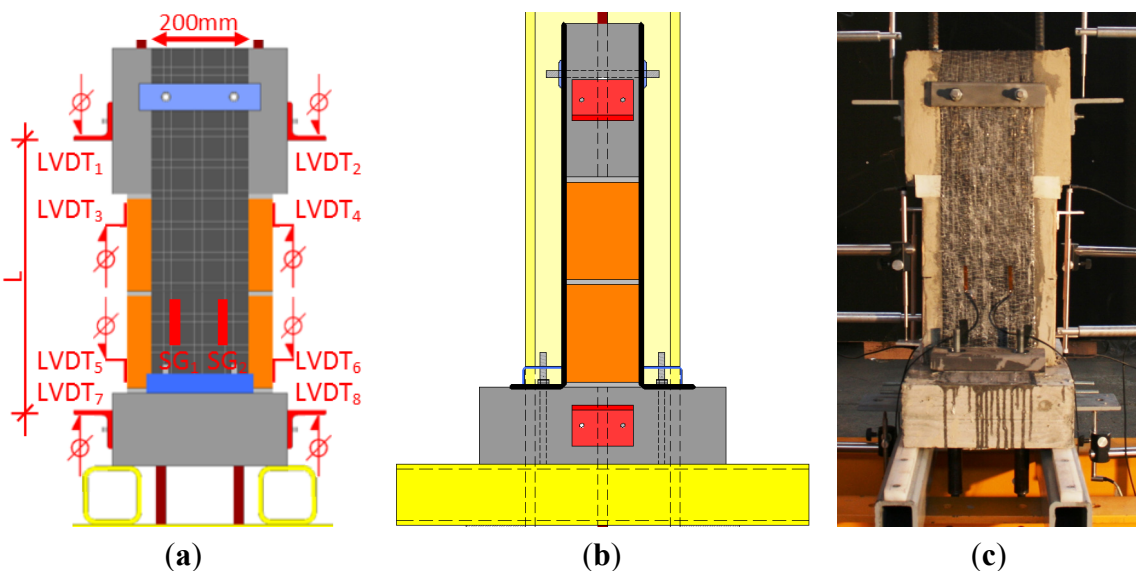


**Table 9.** Characteristics of Series AT-C.

Specimen	Type of C-Sheet	Anchorage Profile	Curvature Radius (mm)	Vertical Anchorage in Slab	Horizontal Anchorage in Brick
AT-C1	240-200 g/m <sup>2</sup>	RHS 60/60/5	10.0	2xM12	-
AT-C2	240-200 g/m <sup>2</sup>	RHS 120/120/5	10.0	2xM12	2xM12
AT-C3	240-400 g/m <sup>2</sup>	RHS 120/120/5	10.0	2xM16	2xM12
AT-C4	240-400 g/m <sup>2</sup>	RHS 120/120/8	16.0	2xM16	2xM12
AT-C5	240-200 g/m <sup>2</sup>	LNP 150/100/10	-	2xM12	2xM12
AT-C6	240-200 g/m <sup>2</sup>	LNP 200/100/10	-	2xM12	2xM12
AT-C7	240-400 g/m <sup>2</sup>	LNP 150/100/10	-	3xM12	2xM12
AT-C8	240-400 g/m <sup>2</sup>	LNP 200/100/10	-	3xM12	2xM12
AT-C9	240-200 g/m <sup>2</sup>	RHS 80/40/8	16.0	2xM12 encased	-

Test Results

The load-displacement curves of Series AT-C are given in Figure 15 (displacement between the concrete block and the aluminum cylinder for AT-C1 to AT-C8 and between the upper and the lower concrete block for AT-C9). The results of Series C are summarized in Table 10.

As can be observed, the test specimens behaved very stiffly at the beginning of the loading process. This is owed to the tensile strength and the stiffness of the mortar connecting the anchored concrete block with the masonry brick. After the mortar’s tensile failure, the specimens’ stiffness highly depends on the presence of horizontal fasteners and the stiffness of the vertical anchorage (mechanical fastener for specimens AT-C1 to C8 or encased by steel rods for C9). This is due to the different behavior of the mechanical anchorage under the bending moment, which is provoked by the eccentricity of the loading with respect to the vertical anchorage. If the rotation of the steel profile is not inhibited, either CFRP failure occurs in the curvature of the mechanical anchorage or concrete failure is the limiting factor. Horizontal fasteners can possibly increase the load that can be anchored. However, they raise new system weaknesses and therefore result in a number of different failure types. The failed specimens AT-C1, AT-C2, AT-C3, and AT-C8 with corresponding simplified sketches are shown in Figure 16.

**Figure 15.** Load-displacement curves of Series AT-C. (a) RHS profiles; (b) L-profiles.

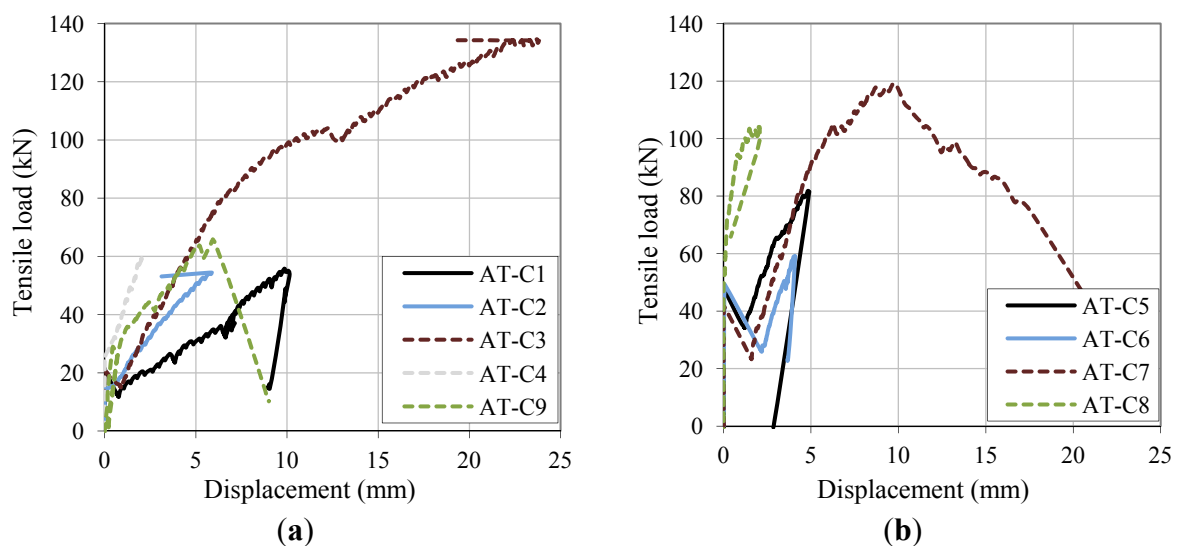


**Table 10.** Results of Series AT-C.

Specimen	$F_{\max}$ (kN)	$F_{\max}/R_u$ <sup>1</sup> (-)	$\sigma_{\max}$ (N/mm <sup>2</sup> )	$\delta(F_{\max})$ <sup>2</sup> (mm)
AT-C1	56	0.21	795	9.9
AT-C2	54	0.20	775	5.7
AT-C3	136	0.25	968	26.1
AT-C4	59	0.11	423	2.0
AT-C5	82	0.31	1166	4.8
AT-C6	59	0.22	842	4.1
AT-C7	119	0.22	849	9.8
AT-C8	108	0.20	741	2.0
AT-C9	82	0.37	1407	5.9

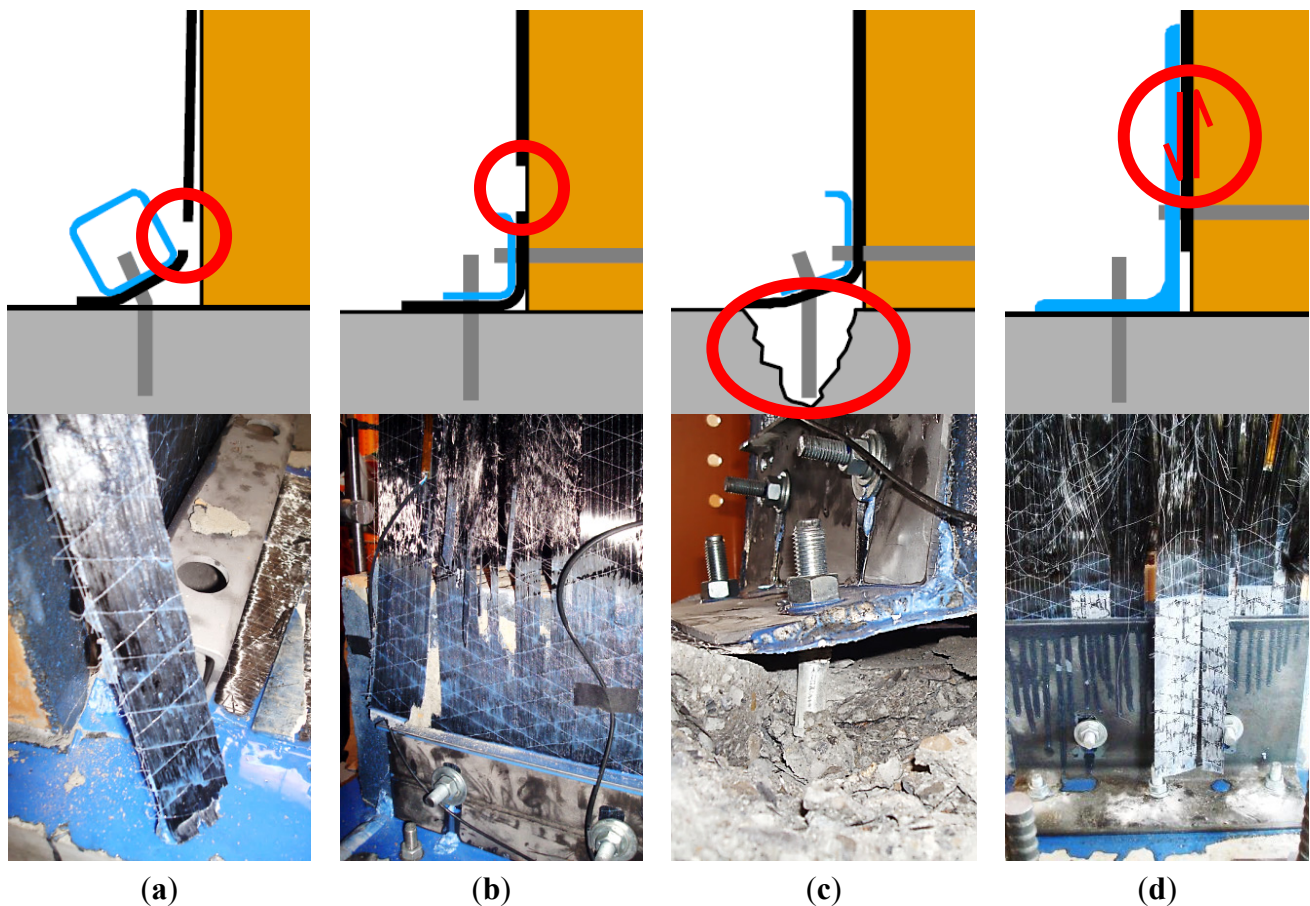
Note: <sup>1</sup>  $R_u$  represents the theoretical ultimate tensile strength of the carbon fibers (fiber rupture).

<sup>2</sup> Displacement measurement between LVDT (1, 2) and fixed concrete block (see Figure 13a) for specimens AT-C1 to AT-C8 and between top LVDT (1, 2) and bottom LVDT (7, 8) (see Figure 14a) for specimen AT-C9.

In Series AT-C, three different failure types occurred:

1. Rupture of CFRP sheet due to stress concentrations at the curvature (AT-C1), at the edge of the steel profile (AT-C2, AT-C6, AT-C9), or at the edge of the masonry brick (AT-C4, AT-C5): Changes of the fiber direction, edges, or bonding defects (e.g., by adhesive accumulation) causing stress concentrations or non-uniform stress distribution along the CFRP sheet lead to highly loaded fibers and, in most cases, subsequently to premature failure. In specimen AT-C1, failure caused by diverting stresses perpendicular to the fiber direction happened in the curvature of the steel profile. Already little deformation of the mechanical fasteners caused a rotation of the anchoring steel profile. This rotation triggered immediate debonding due to peeling. Numerical analyses on mixed-mode bond behavior of [42] have shown that bond shear capacity already drops drastically with small inclinations. Only the bonded joint between the CFRP sheet and the lower horizontal part of the steel profile allowed a further increase of the applied load. In specimens AT-C2, AT-C4, AT-C5, AT-C6, and AT-C9, edges or bonding defects caused premature CFRP failure.
2. Anchorage failure with fracture cone in concrete due to fastener load (specimens AT-C3, AT-C7): As the anchorage strength in the concrete can only be enhanced to limited extents, the limited anchorage capacity in the concrete can significantly diminish the performance of mechanical anchorages for retrofitted masonry walls.
3. Debonding at vertical part of steel profile (AT-C8): This failure occurred unexpectedly early, compared to the experiment results in Series AT-H. Stress concentrations highly influence the bonding behavior and might therefore be the reason for this premature failure.

**Figure 16.** Failed specimens (a) AT-C1; (b) AT-C2; (c) AT-C3; and (d) AT-C8.



It has been shown in Series AT-C that details enormously influence the behavior of the mechanical anchorage of CFRP sheets. By impeding anchorage failure of mechanical fasteners in the concrete in specimen AT-C9, higher fiber tensile stresses could be reached. No conclusions can be drawn from Series AT-C concerning the influence of the curvature radius of the profile incorporating the mechanical anchorage.

#### 4.3. Analytical Study and Approximate Numerical Investigation

In the experimental Series AT-F and AT-C, it has been shown that the bonded CFRP-to-steel joints govern the ultimate bearing capacity of the mechanical anchorage by means of aluminum or steel profiles. So far, however, very little testing of the bonding behavior of CFRP sheets on metallic adherends has been carried out in the scientific community. In this article, an analytical study and an approximate numerical investigation, both based on knowledge from bonded joints between CFRP plates and steel, were conducted in order to gain a deeper insight in the bonding behavior including the effective bond length, an important parameter for the design of a mechanical anchorage.

The numerical investigation focused on the simple configuration tested in Series AT-H. In Series AT-F, it was observed that the bond surface between CFRP sheet and aluminum is the decisive element for the ultimate load bearing capacity. Therefore, the results of the numerical investigation also give insight into the essential bearing behavior from Series AT-F. In Series AT-C, the turning

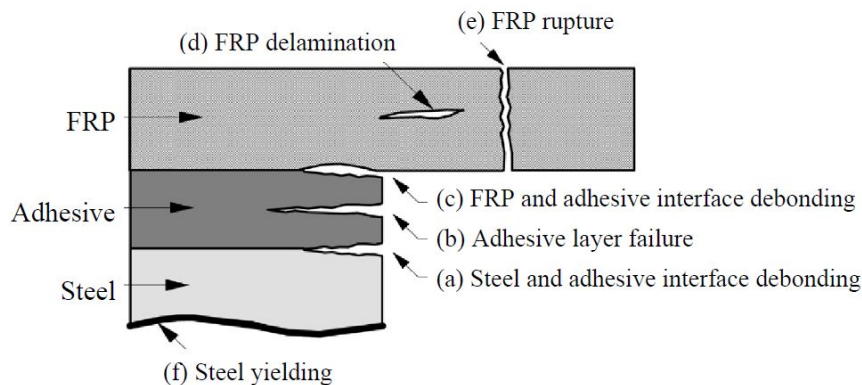


effects and stress concentrations, however, influenced the mechanical anchorage too strongly in order to allow a simple study of the bonding effects.

### 4.3.1. CFRP-to-Steel Bonded Joints

Various failure modes of FRP bonded to steel are possible when the FRP is subjected to tensile loading, as summarized by Zhao and Zhang [43] (see Figure 17).

**Figure 17.** Possible failure modes of FRP bonded to steel [43].



Fernando [41] states that the failure mode “cohesive failure in the adhesive is the preferred mode of debonding failure at CFRP-to-steel interfaces” for CFRP plates. He found in so-called “near-end supported single-shear pull-off tests” that a bi-linear bond-slip model fits the bonding behavior of linear adhesives best. Xia and Teng [44] establish an equation to determine the effective bond length for CFRP plates bonded to steel adherends by means of linear adhesives. They further state that the values for the slip  $\delta_1$  at peak shear stress are generally very small compared to the values of the slip at bond failure  $\delta_f$ . Therefore, they simplify the bilinear bond-slip model assuming a rigid ascending branch followed by a linearly descending branch. The effective bond length  $l_e$  can then be obtained by:

$$l_e = \frac{\pi}{2\sqrt{\frac{\tau_f}{E_p t_p \delta_f}}} \tag{1}$$

$\tau_f$  is the maximum local bond strength and can be calculated through the assumption  $\tau_f = 0.9f_{t,a}$  (according to Fernando [41]), with  $f_{t,a}$  representing the tensile strength of the adhesive.  $E_p$  and  $t_p$  representing Young’s modulus and the thickness of the CFRP plate, respectively, whereas  $\delta_f$  represents the ultimate slip. The ultimate load  $P_{ult}$  of CFRP plates-to-steel bonded joints with a bond length greater than the effective bond length can be found with:

$$P_{ult} = b_p \sqrt{2G_f E_p t_p} \tag{2}$$

where  $G_f$  is the failure interfacial fracture energy of the steel-FRP joint. The interfacial fracture energy can be obtained with a best-fit equation proposed by Fernando [41]:

$$G_f = 628t_a^{0.5} R^2 \tag{3}$$

Here,  $t_a$  represents the thickness and  $R$  the tensile strain energy of the adhesive.  $R$  can be assumed to be equal to the area under the uni-axial tensile stress-strain curve with a linear-elastic material. Therefore, Fernando [41] takes the strain energy to be  $R = f_{t,a}^2 / E_a$ , with  $E_a$  being the elastic modulus of the adhesive. Hence, the slip at failure  $\delta_f$  for linear adhesives can easily be derived by using the form of the bilinear bond-slip model:  $\delta_f = 2G_f/\tau_f$ .

The slip  $\delta_1$  at peak shear stress can be found with a best-fit equation defined by Fernando [41]

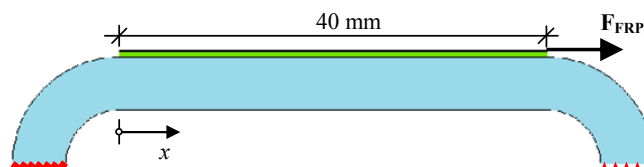
$$\delta_1 = 0.3 \left( \frac{t_a}{G_a} \right)^{0.65} f_{t,a} \quad (4)$$

It is assumed that Equations (1)–(4) hold not only for CFRP plates, but also for CFRP sheets. When applying these equations to the used C-sheet 200 g/m<sup>2</sup> and the used adhesive, a theoretical effective bond length of  $l_e = 20$  mm and an ultimate load of  $P_{ult} = 75.5$  kN corresponding to  $\sigma_{ult} = 2152$  N/mm<sup>2</sup> are obtained.

#### 4.3.2. Basic Numerical Model and Boundary Conditions

The numerical simulations were performed using ABAQUS software [45]. The basic numerical model is based on the mechanical anchorage of test AT-H (Section 4.2.2). The 0.117 mm thick CFRP sheet is bonded on one short side of a rectangular hollow section (RHS) steel profile. Considering the curvature of the steel profile, the bonded length allowing shear transfer corresponds to 40 mm. The adhesive thickness is measured to be approximately 0.5 mm (basic model in Figure 18).

**Figure 18.** Basic numerical model with steel (light blue), adhesive (green), and CFRP (black).



#### 4.3.3. Material Modeling

Three materials were considered for the numerical analysis of FRP-to-steel bonded joints, namely FRP, steel, and adhesive.

The FRP is defined as a linear elastic isotropic material, in accordance to Obaidat *et al.* [46]. The used FRP sheets essentially are unidirectional and, hence, constitute an orthotropic material. However, as loading only occurs in one direction, the Young's modulus in the primary direction is decisive for the results. Therefore, the linear elastic isotropic material is considered suitable. The elastic modulus in the principal direction is 240,000 N/mm<sup>2</sup>. The Poisson's ratio in all directions is assumed to be  $\nu = 0.3$  (as e.g., in [46] or [47]).

For steel, a linear-elastic perfect-plastic and isotropic behavior is assumed. The simulation was carried out for a part of rectangular steel profiles of quality S355. Strain-hardening is neglected. Since the simulations are aimed at studying the bonding interface, the plastic behavior of the steel profile is of secondary importance.

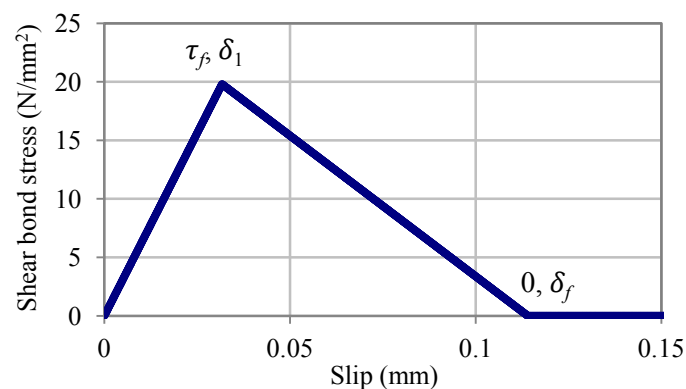


The adhesive is modeled using cohesive elements with uncoupled elastic behavior. The adhesive thickness was measured as  $t_a = 0.5$  mm in all tests with C-sheet 200 g/m<sup>2</sup>. The important material properties used for numerical modeling of the adhesive are:

- Tensile strength  $f_{t,a} = 22.0$  N/mm<sup>2</sup>
- Peak bond stress  $\tau_f = 0.9f_{t,a} = 19.8$  N/mm<sup>2</sup>
- Mode I stiffness  $K_{nm} = E_a/t_a = 9640$  N/mm<sup>3</sup>, being the initial slope of the bond-separation model
- Mode II stiffness  $K_{ss} = K_{tt} = 3(G_a/t_a)^{0.65} = 625$  N/mm<sup>3</sup>, being the initial slope of the bond-slip model
- Fracture energy  $G_{II,F} = 1.13$  N/mm

It is assumed that the adhesive's behavior is linear elastic and, hence, that a bilinear bond-slip model is suitable for modeling the bonding behavior. The bond-slip model used for the numerical simulations and based on the material properties defined above is shown in Figure 19. It is given by the peak shear stress  $\tau_f$  and the corresponding slip  $\delta_1$ , as well as the slip at failure  $\delta_f$ .

**Figure 19.** Shear bond-slip model for bonded CFRP-steel joint.



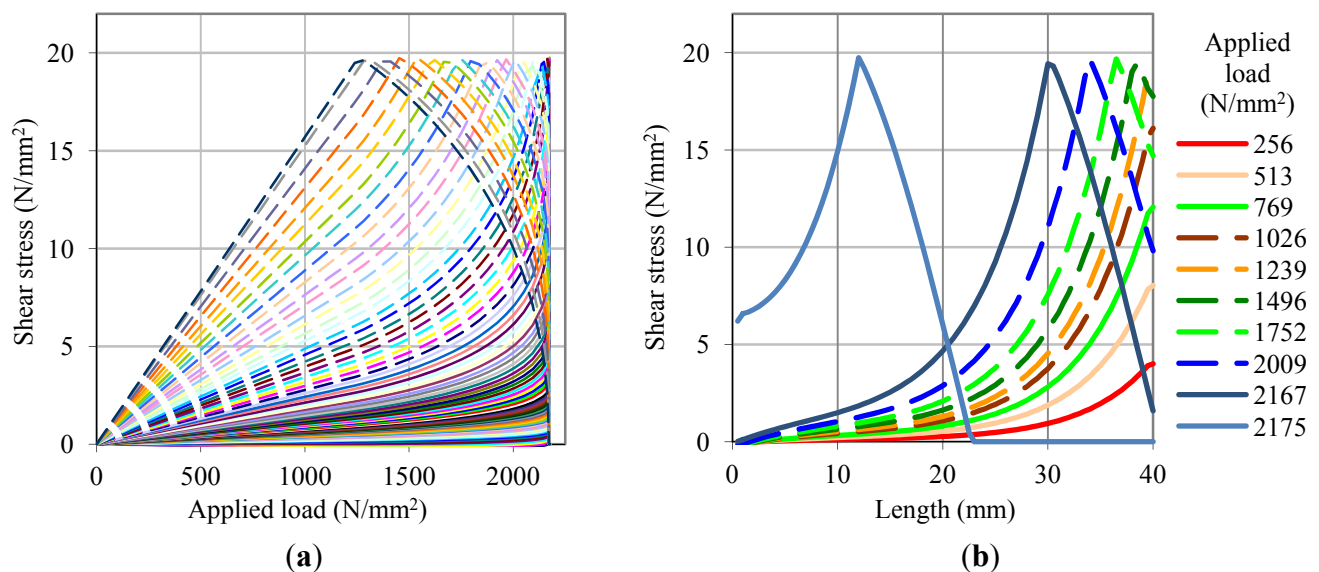
#### 4.3.4. Results of Numerical Simulations

Figure 20a shows the bond shear stress in function of the applied load for every numerical element, distributed over the bonded length. Resulting from the bilinear bond-slip model, the curves in Figure 20b, representing bond shear stress over the length at different stages of applied load, show a hyperbolic behavior until the peak shear stress is reached. When in the softening region, they show a harmonic behavior instead.

It can be seen that up to 2000 N/mm<sup>2</sup>, only the first 3–5 mm of the bonding interface fails. At this point, local failure due to stress concentrations occurs to reduced extents. After debonding initiates, the shear stress transfer propagates and the ultimate bonding capacity is reached very quickly. The curve for an applied load of 2167 N/mm<sup>2</sup> still indicates an intact shear stress transfer, whereas the curve for the maximum applied load of 2175 N/mm<sup>2</sup> depicts a mostly debonded state at failure. Hence, the comparison between the analytical results based on empirical models for CFRP plates and the numerical simulations bring about very similar results. This is to be expected given the fact that the ultimate load mainly depends on the interfacial fracture energy. The fracture energy was considered the same in both, analytical and numerical study. However, the curve for an applied load of 2167 N/mm<sup>2</sup>

seems to show that the effective bond length is higher than the analytically calculated 20 mm, because the shear stress did not reach to zero at 20 mm but at approximately 40 mm. Due to the lack of a valid bond-slip model for CFRP sheet-to-metal-joints, further research including experimental studies and possibly fracture mechanics is required.

**Figure 20.** (a) Bond shear stress for every numerical element along bonding interface in function of applied load. (b) Bond shear stress in function of bond length. Bonding interface is loaded in direction from right to left hand side.



#### 4.4. Comparison between Experimental and Numerical Study

The failure load obtained by the numerical simulations for C-sheets  $200 \text{ g/m}^2$  is very close to the actual failure load. However, for the heavier C-sheets  $240\text{--}400 \text{ g/m}^2$ , the experimental results did not bring about higher failure loads than for the C-sheets  $240\text{--}200 \text{ g/m}^2$ , as the analytical equations would suggest. Concerning the FRP-to-concrete interfaces [34] the normal and shear stresses at the bonded interface increase with the thickness of the FRP. From both the experimental and the numerical study, it can be concluded that the effective bond length of CFRP sheets on metallic adherends is rather short. Thus, in order to study the bond-slip behavior of bonded CFRP sheets-to-steel joints in more detail and to provide adjusted analytical models for bonded CFRP sheets, a more intensive instrumentation for experiments adjusted to the short effective length is required.

## 5. Conclusions

This paper reports the outcomes of an experimental campaign aiming to quantify the seismic capacity of URM walls, the benefit of CFRP retrofitting, and the influence of anchorage in the performance of the retrofitting solution. The results of these tests are valuable in engineering practice as they discuss in detail the effectiveness of a frequently used solution, which nonetheless is very infrequently tested. The outcome of this experimental series serves in establishing some guidelines in the proper setup and anchoring of the CFRP sheets.

The results of the experimental series MR-B show that the tested masonry walls can be retrofitted with CFRP sheets in order to increase the horizontal load capacity by 10%–70% and the deformation capacity by 2%–10%, depending on the configuration of CFRP sheets. Vertically applied sheets increase the bending strength and assist in resisting rocking effects whereas diagonally applied sheets strongly enhance the shear capacity. By applying CFRP sheets or carbon meshes as reinforcement to masonry walls, a new inner state of stress is generated. The reinforcement acts as a tension strut, whereas the masonry acts as a compression strut. The analysis of this tension and compression strut creates the possibility to design according to the truss analogy or according to stress fields.

The static tensile tests conducted on the mechanical anchorage of CFRP sheets show that the effectiveness of the tested materials and configurations largely relies upon details. The sensitivity of the CFRP sheet to edges, non-uniformities on any adherend, inconsistencies of bond stress (e.g., abrupt change from steel to polystyrene), and bonding defects can cause premature CFRP failure and, hence, pose problems for the design of a retrofit. Especially for the configuration tested in Series AT-C, these problems cannot be satisfactorily controlled. Nevertheless, the results in Series AT-H and Series AT-F show that effective anchorage can be achieved when eccentric loading of the mechanical anchorage is avoided and a smooth bonding surface is guaranteed. From Series AT-H, it can be concluded that the bonded length of 40 mm is sufficiently long for both CFRP sheets used. This conclusion was confirmed by numerical simulations and analytic considerations. However, the bonding behavior of bonded CFRP sheet-to-metal joints was not studied in detail and further research is required.

In Series AT-F, anchorage was reliably achieved (for anchorage design see Figure 9c). It was established that the mortar between concrete and masonry influences the specimens' stiffness up to its failure. Bonded joints between the CFRP sheets and the metallic mechanical anchorage as well as between the CFRP sheets and concrete interact until the concrete fails. Consequentially, the tensile strength of CFRP sheets is better exploited by metallic mechanical anchorage than by anchorage on concrete or masonry only.

## Acknowledgments

The presented experiments were conducted within the research project AGP 21159 “Seismic retrofit of masonry structures”. The authors thank the following institutions, research funds, and companies for funding this project: Federal Office for the Environment (FOEN); Research fund of University of Applied Sciences and Arts Western Switzerland (HES SO); S&P Clever Reinforcement Company AG, Seewen SZ; Union des Fabricants de Produits en Béton de Suisse Romande; Brick manufacture Morandi Frères AG, Corcelles près Payerne; Brick manufacture Freiburg & Lausanne AG, Düringen; Fixit AG, Bex (all Switzerland).

## Author Contributions

All authors have contributed to the idea, the planning and the execution of the experimental program which has been carried out under the lead of René Suter. The experimental results have been analyzed and elaborated by Patrick Bischof. The article has been written by Patrick Bischof and Eleni Chatzi.

## Conflicts of Interest

The authors declare no conflict of interest.

## References

1. *Evaluation Of Earthquake Damaged Concrete And Masonry Wall Buildings: Basic Procedures Manual*; FEMA 306; Federal Emergency Management Agency (FEMA): Washington, DC, USA, 1999.
2. Paulay, T.; Priestley, M.J.N. *Seismic Design of Reinforced Concrete and Masonry Buildings*; Wiley: New York, NY, USA, 1992.
3. Salmanpour, A.; Mojsilovic, N.; Schwartz, J. Deformation capacity of unreinforced masonry walls subjected to in-plane loading: A state-of-the-art review. *Int. J. Adv. Struct. Eng.* **2013**, *5*, 1–12.
4. Binda, L.; Chesi, C.; Parisi, M.A. Seismic damage to churches: Observations from the L’Aquila, Italy, earthquake and considerations on a case-study. *Adv. Mater. Res.* **2010**, *133–134*, 641–646.
5. Dizhur, D.; Ingham, J.; Moon, L.; Griffith, M.; Schultz, A.; Senaldi, I.; Magenes, G.; Dickie, J.; Lissel, S.; Centeno, J.; *et al.* Performance of masonry buildings and churches in the 22 February 2011 Christchurch earthquake. *Bull. N. Z. Soc. Earthq. Eng.* **2011**, *44*, 279–296.
6. Gattulli, V. Advanced applications in the field of structural control and health monitoring after the 2009 L’Aquila earthquake. In *Engineering Seismology, Geotechnical and Structural Earthquake Engineering*; D’Amico, S., Ed.; InTech: Rijeka, Croatia, 2013.
7. Gattulli, V.; Antonacci, E.; Vestroni, F. Field observations and failure analysis of the Basilica S. Maria di Collemaggio after the 2009 L’Aquila earthquake. *Eng. Fail. Anal.* **2013**, *34*, 715–734.
8. Augenti, N.; Nanni, A.; Parisi, F. Construction Failures and Innovative Retrofitting. *Buildings* **2013**, *3*, 100–121.
9. Ceci, A.M.; Contento, A.; Fanale, L.; Galeota, D.; Gattulli, V.; Lepidi, M.; Potenza, F. Structural performance of the historic and modern buildings of the University of L’Aquila during the seismic events of April 2009. *Eng. Struct.* **2010**, *32*, 1899–1924.
10. Whittaker, A.; Constantinou, M.; Tsopeles, P. Displacement Estimates for Performance-Based Seismic Design. *J. Struct. Eng.* **1998**, *124*, 905–912.
11. Fardis, M.N. *Advances in Performance-Based Earthquake Engineering*; Springer: Berlin, Germany, 2010; p. 486.
12. Tomaževič, M.; Velechovsky, T. Some aspects of testing small-scale masonry building models on simple earthquake simulators. *Earthq. Eng. Struct. Dyn.* **1992**, *21*, 945–963.
13. *Swisscodes for Engineers*; Schweizerische Ingenieur-und Architektenverein (SIA): Zurich, Switzerland, 2003.
14. Wenk, T. *Einführung in die Erdbebenbemessung mit den neuen Tragwerksnormen*; Swiss Society for Earthquake Engineering and Structural Dynamics: Zurich, Switzerland, 2004. (In German)
15. Triantafyllou, S.P.; Chatzi, E.N. A Novel Hysteretic Multiscale Finite Element Method for Nonlinear Dynamic Analysis of Heterogeneous Structures. In Proceedings of the 11th International Conference on Structural Safety & Reliability, Columbia University, New York, NY, USA, 16–20 June 2014.

16. Parisi, F.; Augenti, N. Uncertainty in Seismic Capacity of Masonry Buildings. *Buildings* **2012**, *2*, 218–230.
17. Lourenço, P.; Avila, L.; Vasconcelos, G.; Alves, J.P.; Mendes, N.; Costa, A. Experimental investigation on the seismic performance of masonry buildings using shaking table testing. *Bull. Earthq. Eng.* **2013**, *11*, 1157–1190.
18. Schwegler, G. Verstärken von Mauerwerk mit Faserverbundwerkstoffen. Ph.D. Thesis, Eidgenössische Technische Hochschule Zürich (ETHZ), Zürich, Switzerland, 1994. (In German)
19. Triantafillou, T. Composites: A New Possibility for the Shear Strengthening of Concrete, Masonry and Wood. *Compos. Sci. Technol.* **1998**, *3538*, 1285–1295.
20. ElGawady, M.; Lestuzzi, P.; Badoux, M. In-Plane Seismic Response of URM Walls Upgraded with FRP. *J. Compos. Constr.* **2005**, *9*, 524–535.
21. ElGawady, M.; Lestuzzi, P.; Badoux, M. Static Cyclic Response of Masonry Walls Retrofitted with Fiber-Reinforced Polymers. *J. Compos. Constr.* **2007**, *11*, 50–61.
22. Prota, A.; Manfredi, G.; Nardone, F. Assessment of Design Formulas for In-Plane FRP Strengthening of Masonry Walls. *J. Compos. Constr.* **2008**, *12*, 643–649.
23. Kalali, A.; Kabir, M.Z. Cyclic behavior of perforated masonry walls strengthened with glass fiber reinforced polymers. *Sci. Iran.* **2012**, *19*, 151–165.
24. Fuggini, C.; Chatzi, E.; Zangani, D. Combining Genetic Algorithms with a Meso-Scale Approach for System Identification of a Smart Polymeric Textile. *Comput. Aided Civil Infrastruct. Eng.* **2013**, *28*, 227–245.
25. Mojsilović, N.; Kostić, N.; Schwartz, J. Modeling of the behaviour of seismically strengthened masonry walls subjected to cyclic in-plane shear. *Eng. Struct.* **2013**, *56*, 1117–1129.
26. Triantafillou, T.; Fardis, M. Strengthening of historic masonry structures with composite materials. *Mater. Struct.* **1997**, *30*, 486–496.
27. Zhuge, Y. FRP-Retrofitted URM Walls under In-Plane Shear: Review and Assessment of Available Models. *J. Compos. Constr.* **2010**, *14*, 743–753.
28. S&P Clever Reinforcement Company Seismic References/Pictures. Available online: <http://www.reinforcement.ch/products/frp-tragwerkverstaerkung/anwendungsbereiche-referenzen/> (accessed on 3 January 2014).
29. Suter, R.; Broye, A.; Grisanti, M. *Essais de Cisaillement de murs en Maçonnerie Renforcés, Série Expérimentale Pluriels MR-A, MR-B, MR-C*; University of Applied Sciences (UAS): Fribourg, Switzerland, 2010. (In French)
30. Bischof, P.; Suter, R. Retrofitting Masonry Walls with Carbon Mesh. *Polymers* **2014**, *6*, 280–299.
31. Kalfat, R.; Al-Mahaidi, R.; Smith, S. Anchorage Devices Used to Improve the Performance of Reinforced Concrete Beams Retrofitted with FRP Composites: State-of-the-Art Review. *J. Compos. Constr.* **2013**, *17*, 14–33.
32. Grelle, S.; Sneed, L. Review of Anchorage Systems for Externally Bonded FRP Laminates. *Int. J. Concr. Struct. Mater.* **2013**, *7*, 17–33.
33. Ceroni, F.; Pecce, M.; Matthys, S.; Taerwe, L. Debonding strength and anchorage devices for reinforced concrete elements strengthened with FRP sheets. *Compos. Part B* **2008**, *39*, 429–441.
34. Nigro, E.; di Ludovico, M.; Bilotta, A. Experimental Investigation of FRP-Concrete Debonding under Cyclic Actions. *J. Mater. Civ. Eng.* **2011**, *23*, 360–371.

35. Fernando, D.; Teng, J.; Yu, T.; Zhao, X. Preparation and Characterization of Steel Surfaces for Adhesive Bonding. *J. Compos. Constr.* **2013**, *17*, doi:10.1061/(ASCE)CC.1943-5614.0000387.
36. *Technical Data Sheet: S&P C-Sheets*; S&P Clever Reinforcement Company: Seewen SZ, Switzerland, 2014.
37. *S&P Resicem Saturating Resin*; Lab Report; LPM (Labor für Prüfung und Materialtechnologie): Beinwil am See, Switzerland, 2001.
38. Suter, R.; Broje, A. Statisch-zyklische Versuche zum Erdbebenverhalten von Mauerwerkswänden. Available online: <http://www.baufachinformation.de/literatur/2011019020243> (accessed on 4 June 2014).
39. *Guide for the Design and Construction of Externally Bonded FRP Systems for Strengthening URM Structures*; American Concrete Institute (ACI) Committee 440: Farmington Hills, MI, USA, 2008.
40. *Advisory Committee on Technical Recommendations for Construction Guide for the Design and Construction of Externally Bonded FRP Systems for Strengthening Existing Structures*; National Research Committee (CNR): Rome, Italy, 2004.
41. Fernando, D. Bond Behaviour and Debonding Failures in CFRP-Strengthened Steel Members. Ph.D. Thesis, The Hong Kong Polytechnic University, Hong Kong, 2010.
42. De Lorenzis, L.; Zavarise, G., Modeling of mixed-mode debonding in the peel test applied to superficial reinforcements. *Int. J. Solids Struct.* **2008**, *45*, 5419–5436.
43. Zhao, X.-L.; Zhang, L. State-of-the-art review on FRP strengthened steel structures. *Eng. Struct.* **2007**, *29*, 1808–1823.
44. Xia, S.H.; Teng, J.G. Behavior of FRP-to-Steel Bonded Joints. In *International Symposium on Bond Behaviour of FRP in Structures (BBFS 2005)*; Chen, J.F., Teng, J.G., Eds.; International Institute for FRP in Construction: Hong Kong, 2005; pp. 411–418.
45. ABAQUS. *Abaqus Version 6.10 Documentations Collection*; Dassault Systèmes Simulia Corp.: Providence, RI, USA, 2010.
46. Obaidat, Y.T.; Heyden, S.; Dahlblom, O. The effect of CFRP and CFRP/concrete interface models when modeling retrofitted RC beams with FEM. *Compos. Struct.* **2010**, *92*, 1391–1398.
47. Bocciarelli, M.; Colombi, P.; Fava, G.; Poggi, C. Prediction of debonding strength of tensile steel/CFRP joints using fracture mechanics and stress based criteria. *Eng. Fract. Mech.* **2009**, *76*, 299–313.